CrystEngComm

HIGHLIGHT

View Article Online
View Journal | View Issue

Cite this: *CrystEngComm*, 2024, **26**, 11

Durability of S- and N-doped graphene nanoplatelets for electrode performance in solid-state batteries

Vijay Kumar Srivastava,[a] Stefanos Mourdikoudis,*[bd] Jalal Azadmanjiri,*[b] Parshant Kumar[c] and Zdeněk Sofer*[b]

Received 6th November 2023,
Accepted 15th November 2023

DOI: 10.1039/d3ce01111a

rsc.li/crystengcomm

The main emphasis of the present Highlight paper is to summarise reported works aiming to understand the effect of sulfur and nitrogen doping on graphene nanoplatelets for high capacity electrodes in solid-state rechargeable energy storage devices. Lithium-ion batteries are considered to be one of the most promising energy storage devices which have the potential of integrating the high energy granted by lithium-ion batteries and long cycling life of supercapacitors in the same system. However, the present Li-ion batteries provide only high power density due to the low electrical conductivity of the anode materials. Moreover, there is a need to increase the capacity and kinetic imbalances between the anode and cathode by designing high-power and stable structures for the anode and cathode materials. Graphene nanoplatelets (GnPs) have been intensively explored as anode materials in lithium ion batteries due to their unique structure and outstanding electrochemical properties. The synthesis procedure, structure and electrochemical performance of such materials are discussed extensively in this manuscript.

1. Introduction

The last two decades have witnessed a significant advancement in the field of carbon-based nanomaterials for applications in various sectors such as structural,[1] optoelectronics, sensing,[2] and high-end energy applications.[3] Although the chemical make-up may be the same for various carbon-based nanomaterials, the atomic bonding arrangement may vary significantly, given that different carbon-based nanomaterials may yield disparate sets of properties.[4] Furthermore, the use of carbon-based materials is not new in Li-ion batteries. The first use of a carbon-based material occurred in 1985 in Japan[5] when graphite was used as an anode in Li-ion batteries. Its use as an anode in Li-ion batteries was attributed to its incomparable balance of cost, power density, abundance, high energy density (high capacity with low de-/lithiation potential), low volume expansion, high stability, long cycle life, low potential difference between carbon and Li, and excellent electronic and ionic conductivity.[5,6] Various carbon-based materials could be used as electrodes in Li-ion batteries. However, mainly graphite, CNTs, and graphene have been used in Li-ion batteries. In fact, the use of carbon-based materials in Li-ion batteries started in 1985 and the invention timeline of graphite, CNTs, and graphene is shown in Fig. 1.[7–9]

Among the various carbon-based nanomaterials, graphene and carbon nanotubes usually possess the best combination of properties and resulting benefits.[10] However, graphene, which is considered as a wonder material, outperforms carbon nanotubes in several applications.[11,12]

Graphene is the thinnest material in the carbon family and it is a potential candidate for various applications due to its large aspect ratio, ease of obtaining, abundant functional groups, low density, and tunable properties.[13] Even though graphene is being already employed in a variety of applications, its usage in energy storage devices continues to progressively increase to meet the increasing demand of modern electronics and electric vehicles.[14] Furthermore, the fast electron transfer rate, excellent electrochemical activity, high specific surface area (~2630 m^2 g^{-1}), broad electrochemical window, and achievement of high power density with high energy density make graphene a lucrative choice for electrodes of solid state batteries (SSBs).[15–17] SSBs function with the same principle as that of conventional Li-ion batteries with the difference of using solid electrolyte instead of liquid electrolyte; this leads to improvement of the cycle life, reduction in the flammability, and increase in the energy density.[18] Although graphene is an

---

[a] *Department of Mechanical Engineering, Indian Institute of Technology (BHU), Varanasi-221005, India*

[b] *Department of Inorganic Chemistry, University of Chemistry and Technology Prague, Technicka 5, 166 28 Prague 6, Czech Republic. E-mail: mourdikt@vscht.cz, jalal.azadmanjiri@vscht.cz, jalal_azad2000@yahoo.com, soferz@vscht.cz*

[c] *Department of Mechanical Engineering, Dr. Vishwanath Karad MIT World Peace University Pune, India*

[d] *Separation and Conversion Technology, Flemish Institute for Technological Research (VITO), Boeretang 200, Mol, 2400 Belgium*

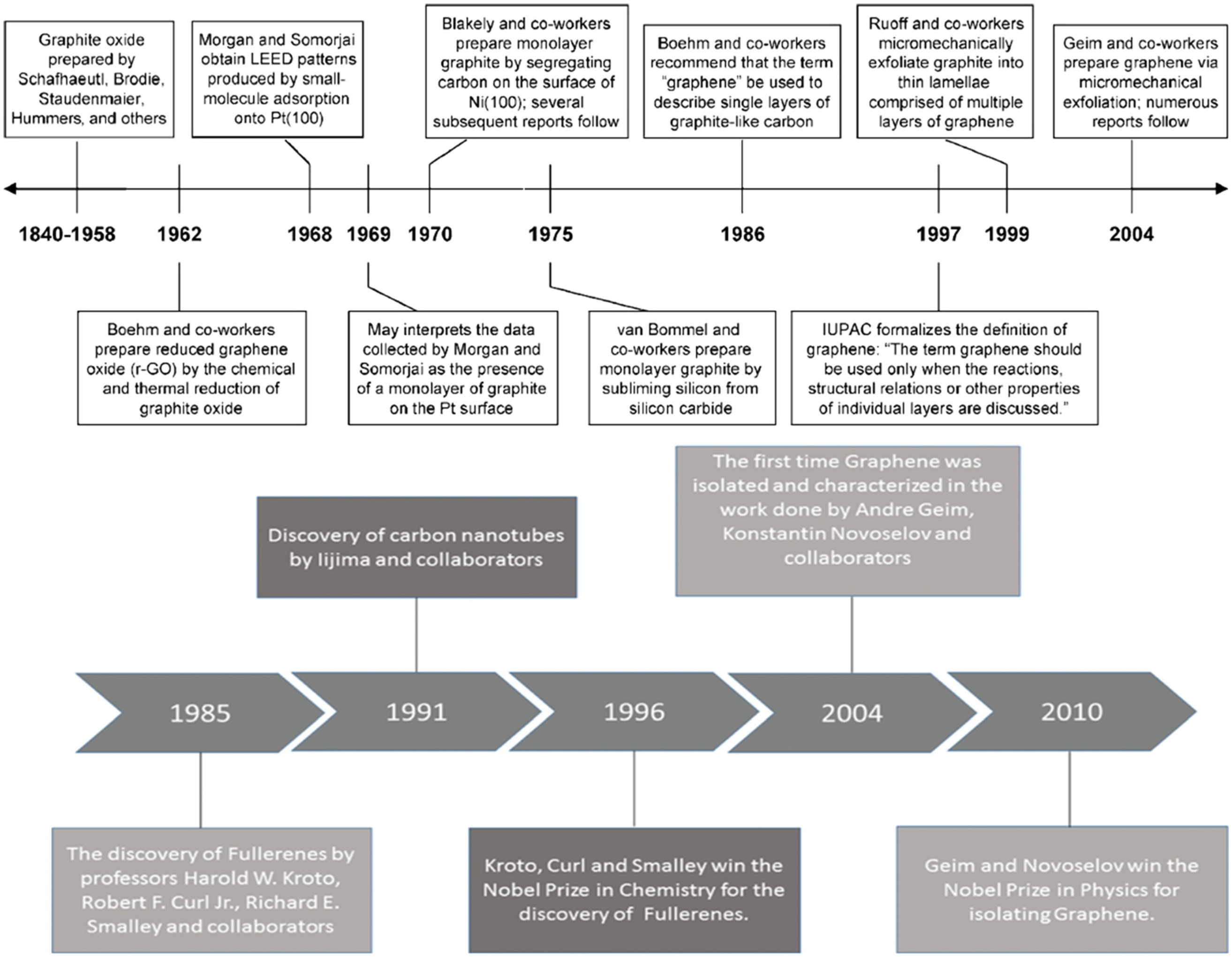

Fig. 1 Invention timeline of graphite, CNTs and graphene;[7–9] 2012, The Royal Society of Chemistry; reprinted with permission, Copyright 2010 Wiley-VCH; 2019 Walter de Gruyter GmbH, published under a CC License (open access).

excellent material for energy storage devices, its performance in batteries can be further improved by precise and reproducible doping which alters the Fermi energy level and tunes the band gap required for the suitable energy storage application.[19] Fig. 2(a–d) show the effect of p-type and n-type doping on the Fermi level and operation mode of graphene. It can be observed from Fig. 2(a) and (b) that pristine graphene is a gapless semiconductor having a Fermi level at the Dirac point of the energy band structure. Doping of either p-type or n-type could shift the Fermi level and create a tunable bandgap between valence and conduction bands.[20] This facilitates the movement of electrons from the valence band to the conduction band which may promote charge transfer (as shown in Fig. 2(c) and (d)) and reduce the energy barrier for ion intercalation. Fig. 2(e) and (f) show the Nyquist plots for undoped and N-doped (nitrogen doped) graphene, before cycling and after 5 cycles, respectively.

It can be observed from Fig. 2(e) that both pristine graphene and N-doped graphene exhibited almost similar resistances before cycling. However after 5 cycles (Fig. 2(f)), when nitrogen was introduced to the basal planes of graphene, N-doped graphene displayed a lower charge resistance and better ionic conductivity. The improved performance of graphene could be attributed to several factors, *i.e.*, i) more lone pair electrons for graphene are produced with the introduction of nitrogen atoms which improved the electron mobility and electronic conductivity, ii) graphene defects are increased with the introduction of nitrogen atoms which facilitated the storage of more ions, iii) due to the higher electronegativity of nitrogen as compared to graphene, the adsorption energy was improved and the energy barrier was decreased for ion intercalation. Thus, doping produces a significant effect on the energy storage potential of batteries.

Although several heteroatoms can be used to dope graphene for energy storage applications, the doping of boron (B), nitrogen (N), and sulfur (S) in the graphene lattice is a popular practice due to several resulting benefits obtained over other dopants.[22,23] Boron doping results in a p-type doping effect on the materials whereas nitrogen doping may result in both p-type and n-type doping effects

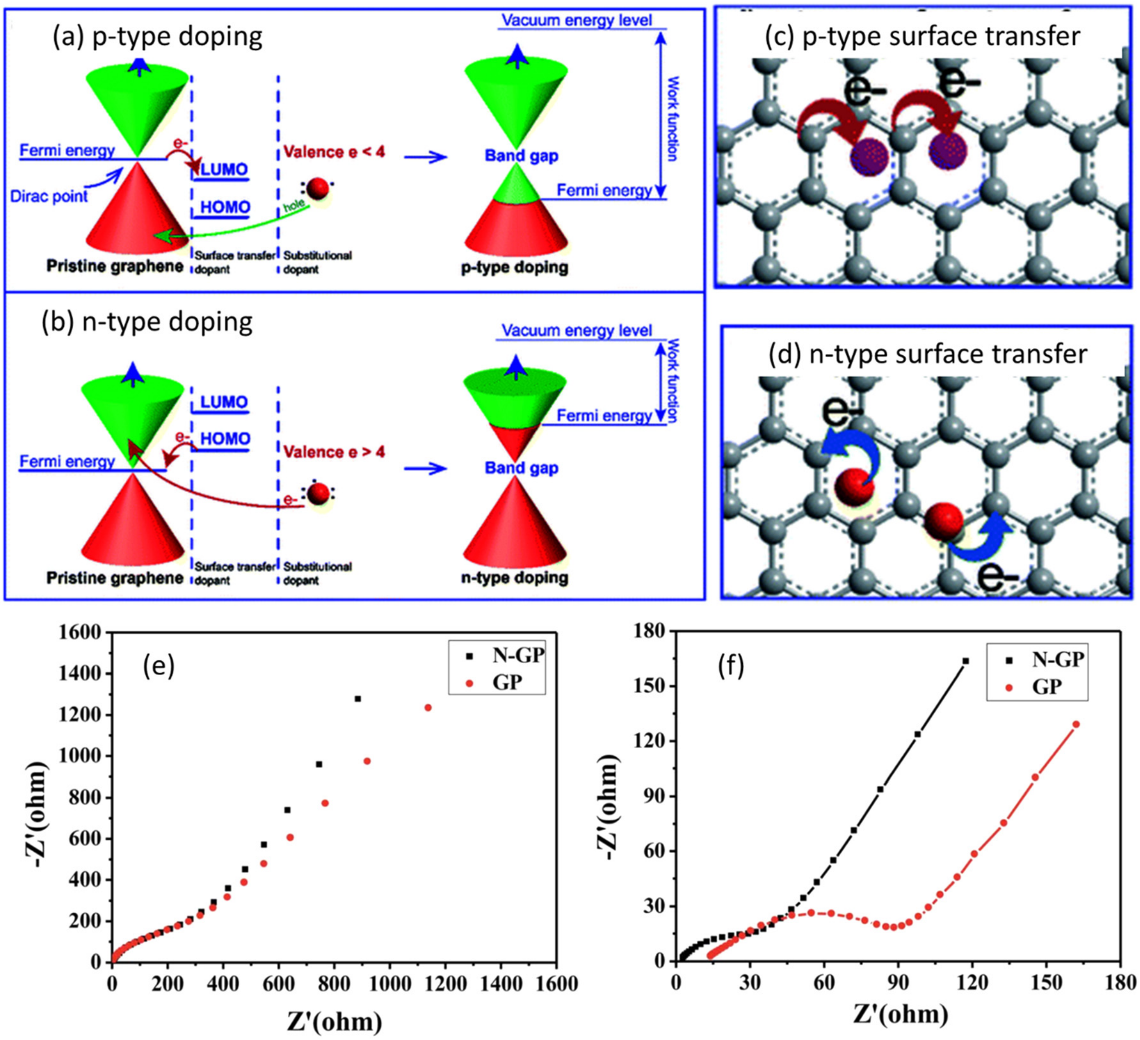

Fig. 2 Illustration of the energy diagram of (a) p-type doped graphene; (b) n-type doped graphene. Structure of doped-graphene by: (c) p-type surface transfer doping; (d) n-type surface transfer doping. Nyquist plots for N-GP and GP (e) before cycling and (f) after 5 cycles with the fitted curves. Panels (a–d) are reproduced with permission from the data published in ref. 20 Copyright 2021, The Royal Society of Chemistry. Panels (e and f) are reproduced with permission from the data published in ref. 21 Copyright 2018, The Royal Society of Chemistry.

which depends upon the type of dominant functional group present in nitrogen. Thus different dopants may lead to distinct electrochemical performances. For instance, Wang *et al.*[24] performed cyclic voltammetry (CV), galvanostatic charge–discharge (GCD) and calculated specific capacitance (Csc) experiments at different current densities, as well as cycling stability studies on S, N, and co-doped graphene. The authors found that co-doped graphene exhibits better electrochemical performance as compared to single doped with sulfur and nitrogen as shown in Fig. 3.

It can be understood from Fig. 3 that S, N, and co-doped graphene exhibit different electrochemical performances due to varying dopant and doping characteristics. Thus the extensive study of dopant morphology, electronic properties, chemical composition, and functional groups is necessary to tailor the doped graphene for energy storage applications.[22] These points constitute the main theme of the present review paper.

2. Graphene as the positive electrode skeleton

Graphene nanoplatelets (GnPs) exhibit particularly high conductivity together with chemical stability. The electrical conductivity of GnPs is affected by the number of graphene layers, shape and size of nanoplatelets. The high value of electrical conductivity mainly arises from the delocalization of electrons over the entire graphene surface which enables the facile movement of electrons. Basically, graphene is a two-dimensional (2D) material which comprises a one-atom-thick sp^2-carbon layer, sharing many similar properties with SWCNTs. When the graphene sheet is rolled at a certain angle, it converts to SWCNTs. Graphene nanoplates can only be used as a three-dimensional (3D) hybrid structure constructed by placing SWCNTs among graphene planes through covalent C–C bonding. Therefore, combining the 1D SWCNTs and 2D graphene into 3D GnPs/SWCNTs hybrids is

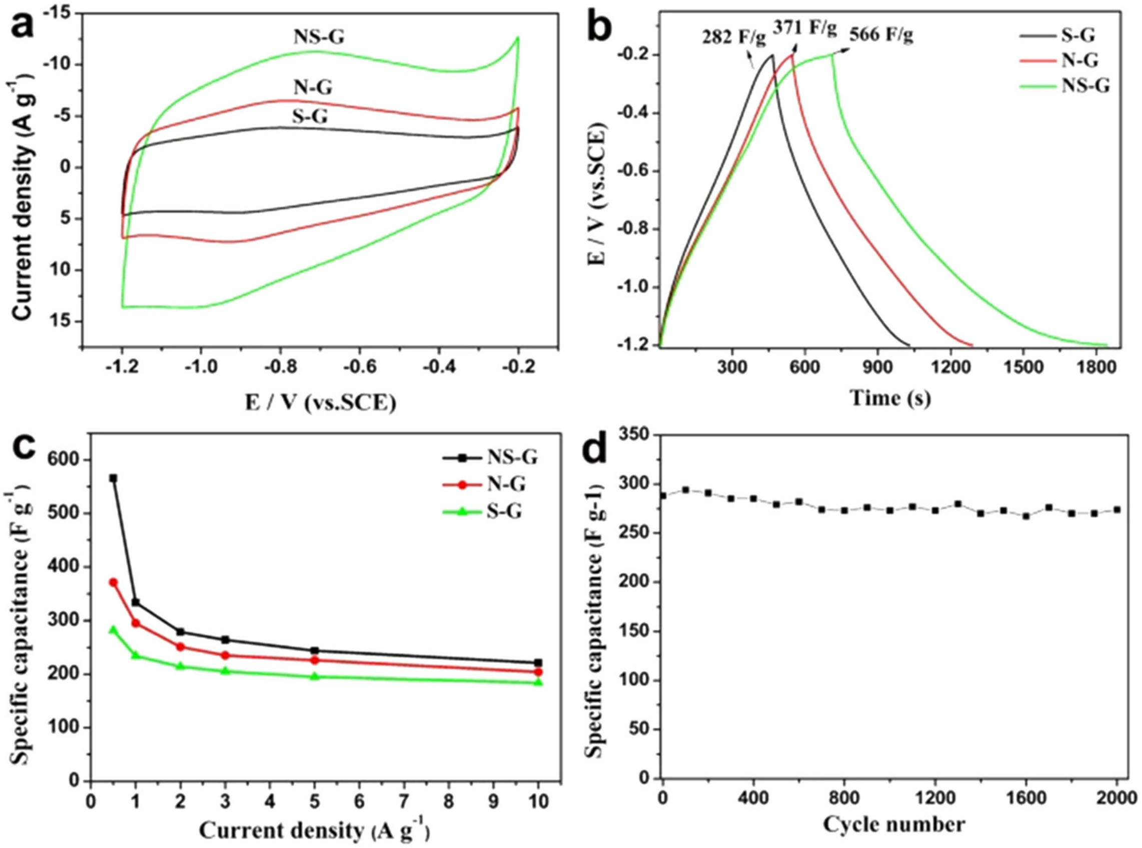

Fig. 3 (a) CVs measured at 30 mV s^{-1} and (b) GCD curves measured at 0.5 A g^{-1} of NS-G, N-G and S-G samples. (c) The specific capacitance of NS-G, N-G and S-G at different current densities and (d) cycle performance of NS-G at a current density of 3.0 A g^{-1}.[24] 2015 Springer Nature, published under a CC license (open access).

considered to be an effective route to bridge microscopic SWCNTs as well as graphene. This approach can further extend the applications of these materials in macroscopic devices through a bottom-up strategy, without introducing any non-carbon impurities. The SWCNTs and graphene can be well distributed in the GnPs/SWCNTs hybrids and effectively connected with reduced interface thermal and electrical resistance. Therefore, several excellent features of the GnPs/SWCNTs hybrids, such as thermal, mechanical, and energy storage properties, have been proposed by theoretical modeling.[25] The strategy for the fabrication of GnPs/SWCNTs hybrids is illustrated in Fig. 4d. Hydrogen helps to reduce the layer of double hydroxides (LDHs) which come from (FeNPs) with extraordinary thermal stability. Consequently SWCNTs can grow continuously from these FeNPs with the constant introduction of hydrocarbons. The hybrid GnPs/SWCNT structure is isolated after removal of the calcined LDH flakes. The fabricated GnPs/SWCNTs hybrids are composed of two portions of the GnPs/SWCNTs hybrid with their graphene layers stacked together because both sides of the LDH flakes were effective for the deposition of graphene and SWCNTs as shown in Fig. 4d.

Generally, during the CVD process, the growth of SWCNTs requires catalyst NPs with small size (<5 nm) for high thermal stability, while the growth of graphene necessitates a continuous flat substrate. Furthermore, achieving rapid growth of SWCNTs on a graphene substrate is extremely difficult: carbon atoms in the graphene sheet can be dissolved into the metal NPs during the precondition process, which results in the quick sintering of metal NPs onto the graphene surface. CNTs grown on the graphene substrate usually have multiwall numbers and much less graphitization.[25] Recently, a one-step fabrication of GnPs/SWCNT hybrids was reported by using a mixed catalyst.[25] Layered double hydroxide (LDH) materials comprise a multifunctional catalyst for the one-step CVD growth of GnPs/SWCNT hybrids. The formation of sp^2 carbon materials from LDHs has been found to be of key importance for the catalysis of the fabrication of GnPs/SWCNT hybrids with extraordinary thermal stability for SWCNT formation based on their layered structure. A CVD process was performed at high-temperature (over 950 °C) using FeMgAl LDH flakes to achieve the *in situ* deposition of both SWCNTs and GnPs/SWCNTs hybrid structures. The prepared FeMgAl layered double hydroxide flakes were well-crystallized hexagonal structures with a lateral size of *ca.* 1 μm and a thickness of several nanometers (Fig. 4a (i)). Calcination of the FeMgAl LDH flakes resulted in dehydration and decarbonization, leading to the formation of the corresponding FeMgAl layered double oxide (LDO) flakes, which were mainly composed of MgO, Fe$_3$O$_4$ and MgAl$_2$O$_4$ (Fig. 4a (ii)). However, the plate-like structure of the LDHs can be well preserved for the FeMgAl (LDO) flakes (Fig. 4a (iii)). The

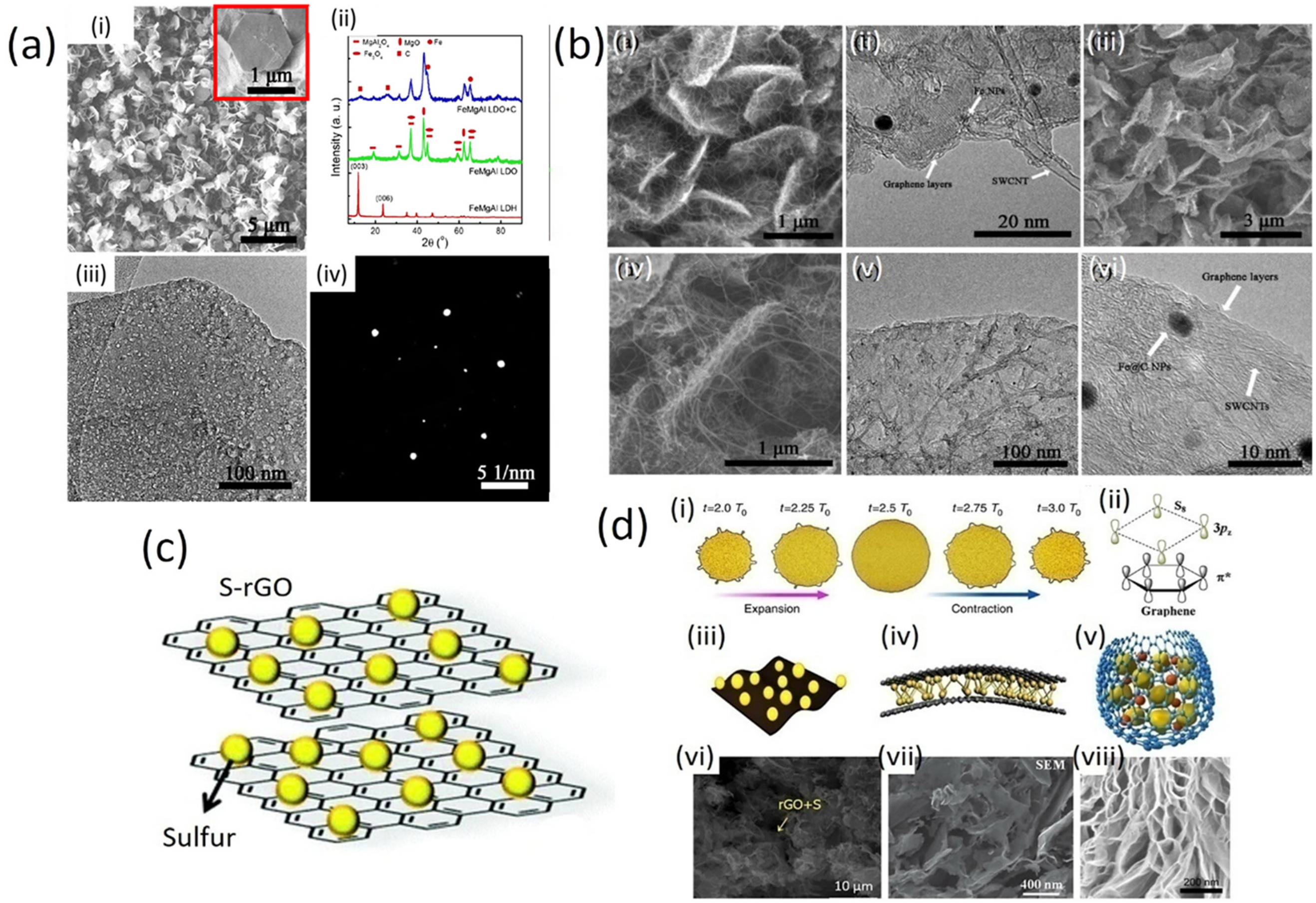

Fig. 4 a) i) SEM image of the as-prepared FeMgAl LDH flakes. The inset image shows a hexagonal LDH flake. (ii) XRD patterns of the FeMgAl LDH and FeMgAl LDO obtained by calcinating FeMgAl LDH at 950 °C for 15 min, and the products after the CVD growth of the G/SWCNT hybrids. (iii) TEM image and (iv) SAED pattern of the FeMgAl LDO flakes (with permission of American Chemical Society 2012);[25] b) (i) SEM and (ii) TEM images of the as-grown GnPs/SWCNT/LDO hybrids; (iii and iv) SEM image of the as-fabricated GnPs/SWCNT hybrids; (v) TEM and (vi) HRTEM image of the GnPs/SWCNT hybrids (with permission from American Chemical Society 2012);[25] c) schematic S/graphene composite for battery cathodes;[26,27] d) interaction between graphene and sulfur and its configuration. (i) Macroscopic volume change of graphene-coated sulfur particles. (ii) Microscopic symmetry and non-polarity of graphene and sulfur. (iii) The in-plane structure has the advantage of flexible electrodes. (iv) Sandwich structure: sulfur is confined between two or more layers of graphene sheets. (v) core–shell structure: sulfur and LiPSs are coated by graphene to prevent leakage. (vi) SEM image of complex of sulfur and graphene oxide (S/GO). (vii) The sandwich structure of sulfur is evenly distributed on the graphene sheet. (viii) SEM image of core–shell structure (published under open access CC VY license, MDPI).[28–31]

FeMgAl LDO flakes had a uniform structure rather than being randomly mixed metal oxides and a clear hexagonal diffraction pattern was identified by selected area electron diffraction as shown in Fig. 4a (iv).[26]

Moreover, methane has been used to serve as a carbon source for the final product of GnPs/SWCNTs hybrid flakes (Fig. 4b (i)). Single- or bi-layer graphene was observed on the surface of the LDO flakes, and SWCNTs grown from the small-sized catalyst NPs embedded in the LDO flakes could also be observed (Fig. 4b (ii)). After the removal of the LDO flakes, the GnPs/SWCNT hybrids exhibited a similar interlinked morphology to that of the G/SWCNT/LDO nanocomposites (Fig. 4b (iii) and (iv)), in which most of the SWCNTs grew onto the surface of graphene layers at both sides. TEM images show the morphology and composition of few-layers of graphene and SWCNTs with few graphene layers encapsulating Fe NPs (Fe@C NPs), as depicted in Fig. 4b (v) and (vi).

2.1 The interactions between sulfur and graphene

Many recent reports on sulfur-embedded carbon cathodes mention that significant reduction of lithium sulfur batteries can take place. Carbon materials come with an excellent conductive scaffold and flexible structure such as graphene and carbon nanotubes (CNTs) with a diverse morphology, which can function efficiently as the sulfur and polysulfide confinement cage in cathodes for the Li–S battery system. Graphene oxide (GO) offers a promising solution as a host in Li–S cathodes and S/graphene composites. In GO/sulfur composites, graphene plays a significant role in improving the electronic conductivity of sulfur, inhibiting the shuttle effect of soluble polysulfides that causes cathode cracking in traditional cathodes. GO-based cathodes have been shown to be more durable and efficient than traditional ones in lithium-sulfur battery technology because GO has various functional groups due to which it is able to chemically bond with polysulfides, endowing GO with a strong polysulfide entrapping ability.[32]

The physical and chemical interactions between sulfur molecules and graphene show that the geometric features of graphene allow it to serve as a substrate material for coating sulfur particles on a macroscopic scale as illustrated in Fig. 4d (i–iii). The stretching ability of the sulfur cathode framework is essential for the improvement of electrochemical performance. In fact, graphene boosts the charge transfer between sulfur particles and electrolytes due to its unique structure. The physical coating of graphene can prevent the spreading of dissolved polysulfides. Porous graphene can accommodate the volume expansion and improve the utilization of sulfur during the charge–discharge process. Moreover, the graphene hexagonal honeycomb lattice structure is composed of carbon atoms with sp^2-hybridisation orbitals. The S_8 molecule has a zig-zag ring with eight sulfur atoms, which is called a double-layer octagonal structure.[32] The crystal structures of graphene and elemental S_8 molecules are both highly symmetrical and they display non-polar properties, as shown in Fig. 5d (iv and v). Therefore, van der Waals forces are very strong. The interaction between the two species is reflected in the pairs of S $3p_z^2$ electrons and the antibonding conjugated states of the graphene plane. The graphene-based materials are bonded to the element of the S_8 molecule. Hence, lithium polysulfide (LiPS), depicted in Fig. 5d (vi–viii)[28] is a suitable choice for the sulfur cathode framework.

Fig. 5a (i) shows that during the first four cycles of the cyclic voltammogram profiles, no changes can be observed for both the anodic/cathodic peaks implying the electrochemical stability of the cathode. The cycling stability of the GnPs/SWCNTs hybrid nanocomposites is demonstrated in Fig. 5a (ii). Two discharge plateaus

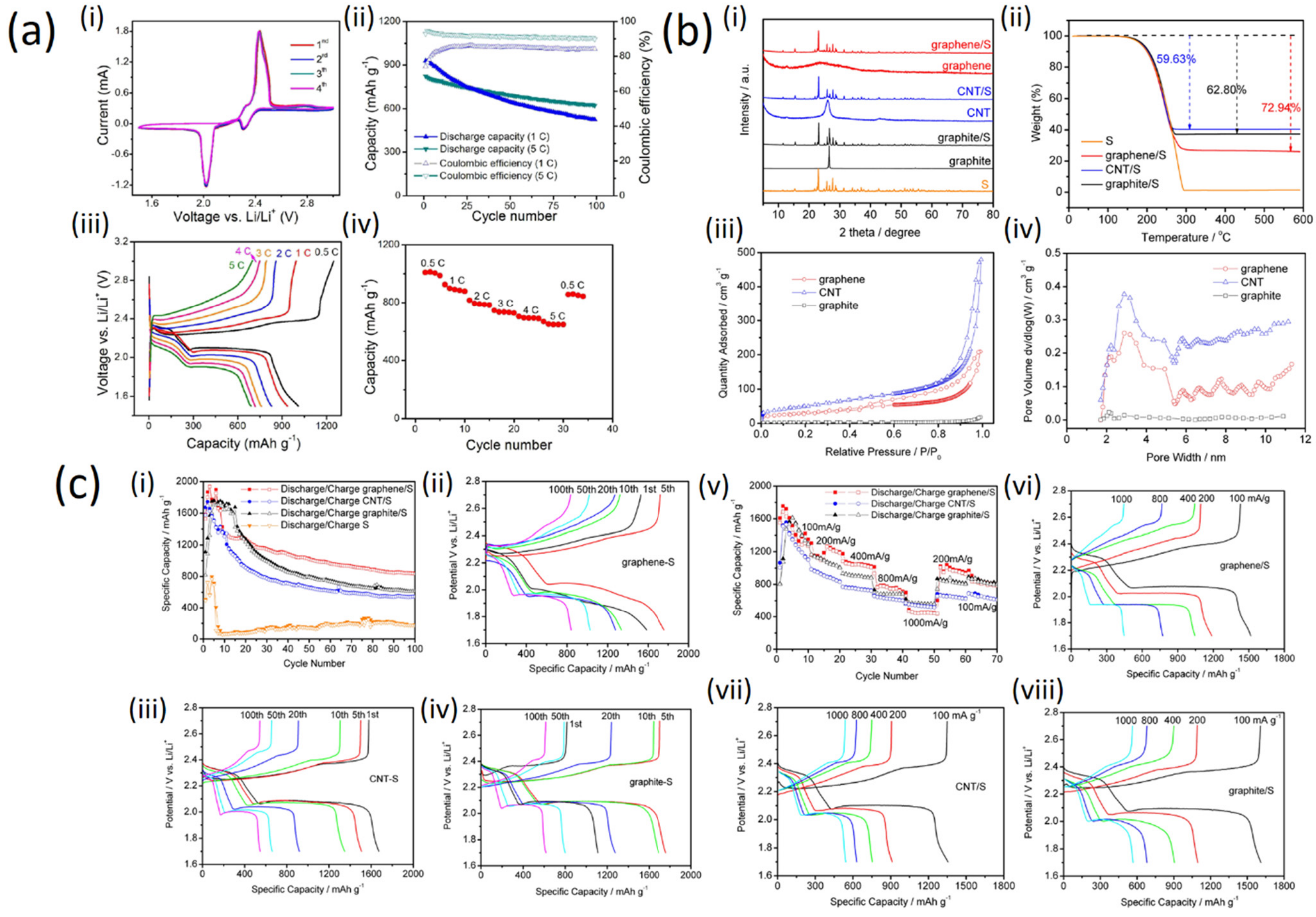

Fig. 5 a) Electrode performance of the GnPs/SWCNT-S nanocomposites for Li–S cells: (i) CV profiles; (ii) cycling stability; (iii) galvanostatic charge–discharge curves at different current rates; (iv) rate performance (with permission from American Chemical Society 2012);[25] b) (i) XRD patterns of graphene, CNT, graphite, graphene/S, CNT/S, graphite/S, and pure sulfur materials; (ii) TGA analysis of the graphene/S, CNT/S, graphite/S, and pure S materials, nitrogen protected, 20 °C min^{-1} heating rate; (iii) isotherms for N_2 adsorption–desorption on graphene, CNT, and graphite materials; (iv) BJH graphene, CNT, and graphite pore-size distribution (with permission from American Chemical Society 2019); c) (i) cycle performances of graphene/S, CNT/S, graphite/S, and pure sulfur cathodes, current density is 200 mA g^{-1}; specific capacity potential plots for (ii) graphene/S, (iii) CNT/S, and (iv) graphite/S at different cycles; (v) high-rate performance of the graphene/S, CNT/S, and graphite/S cathodes; plots of specific capacity potential for (vi) graphene/S, (vii) CNT/S, and (viii) graphite/S cathode at different high-rate charge/discharge current densities (with permission from American Chemical Society 2019).[33]

corresponding to the reduction of S to high-order lithium polysulfides and to Li_2S_2 and Li_2S, respectively, were observed for all the discharge curves at different current rates as shown in Fig. 5a (iii). However, a high reversible capacity of *ca.* 650 mA h g^{-1} can be still preserved even at the very high current rate of 5C, indicating an excellent rate performance of the GnPs/SWCNT-S nanocomposites as depicted in Fig. 5a (iv). This demonstrates that the sulfur in the GnPs/SWCNT-S cathodes can be fully utilized at every current rate.

To compare the effect of sulfur on graphene, graphite and CNTs, sulfur-embedded carbon cathodes were prepared with carbon allotropes of graphene. X-ray diffraction (XRD) patterns of graphene, CNT, graphite, graphene/S, CNT/S, graphite/S and pure S materials are shown in Fig. 5b (i). There is no distinct peak in the XRD pattern of graphene, which indicates low crystallinity or amorphous structure. The XRD diffraction peaks of CNTs and flake graphite are located at 26.5°, in accordance with what is expected for the typical structure of graphite crystals.[33] The thermogravimetric analysis (TGA) shows the effect of sulfur on graphite structure (Fig. 5b (ii)), indicating the weight loss of pure S in the temperature range 190–300 °C. In the same temperature range, the three carbon/S composites reproduce the weight loss profile of pure sulfur; this serves as a good approximation for the determination of the sulfur weight ratio in the composites. Therefore, the weight losses of S in the graphene/S, CNT/S, and graphite/S are calculated as 72.94, 59.63, and 62.80 wt%, respectively. The porosity of the three carbon/S composites was determined by adsorption–desorption isotherms with N_2, as shown in Fig. 5b (iii). With relative pressure ranging from 0.8 to 1.0, all three samples demonstrate no hysteresis loop, suggesting that these materials have a large number of homogeneous pores. The distribution of the pore size can be deduced with Barrett–Joyner–Halenda (BJH)'s adsorption variants, as shown in Fig. 5b (iv).

Furthermore, electrochemical characterization was applied to estimate the function of the three carbon/S cathodes with metallic lithium as the anode. The long-term stability for cycling up to 100 cycles with 200 mA g^{-1} current density is shown in Fig. 5c (i and ii) where all three cathodes exhibit better cycle stability than pure sulfur. Among the three cathodes, the discharge capacity of graphene/S remains above 840 mA h g^{-1} for up to 100 cycles. Moreover, the average coulombic efficiency of the graphene/S cathode is revealed to be >99.4%, which demonstrates the best cycle stability and excellent reversibility. The increase in capacity during the first few cycles is because of the electrode activity process. The lithium ion gradually enters the electrode materials, so the lithiation channels become much smoother after the first few cycles resulting in increasing capacity. Fig. 5c (iii) and (iv) present the cycle dependence of charge/discharge performance for the three carbon/S cathodes. The CNT/S cathode is capable of delivering a high capacity from the very beginning, while graphene/S and graphite/S capacity peaks can only be obtained after 10–20 warm-up cycles, which indicates that the CNT/S cathode displays the fastest electrochemical active kinetics among the tested cathodes. The rate capability, for all of them, was estimated in a wide range of current density. As can be seen from Fig. 5c (v and vi), the graphene/S cathode exhibits a high discharge capacity of 1600 mA h g^{-1} in the first few cycles at a current density of 100 mA g^{-1}. When current density was elevated to 200, 400, 800, and 1000 mA g^{-1}, the cathodes exhibited capacities of 1196, 1023, 713, and 448 mA h g^{-1}, respectively. Furthermore, the graphene/S cathode shows good recovery of the capacity of 945 and 798 mA g^{-1} as the current rate drops to 200 and 100 mA g^{-1}. It is worth mentioning that CNT/S and graphite/S cathodes have better capacities of 518 and 557 mA h g^{-1} than the graphene/S cathode when it comes to a high current rate (1 A g^{-1}), which can be explained by the fact that CNTs and graphite provide faster sulfur utilization under high rate charge/discharge conditions. Fig. 5c (vii and viii) displays the charge rate dependence of charge/discharge behaviors of the three carbon/S cathodes. There are two prominent plateaus at the high charge rate which denote excellent electrical conductivity resulting in rapid charge transfer.[32,34]

Fig. 6a shows the charge–discharge voltage profiles of the 11th cycle measured during galvanostatic cycling at 0.1C (where 1C corresponds to a current density of 1675 mA g^{-1}) within 1.5–3.0 V (*vs.* Li^+/Li). As it can be observed, two plateaus at 2.35 V and 2.05 V were clearly visible during the discharge process, which correspond to the formation of long-chain lithium polysulfides (Li_2S_x, $4 \leq x \leq 8$) and short-chain lithium polysulfides (such as Li_2S_2 and Li_2S), respectively. Such a discharge profile is common for sulfur cathodes. On the basis of the discharge results, the S-GS electrode was able to deliver 6.0 mA h cm^{-2} of the electrode and 625 mA h g^{-1} of sulfur in the 11th discharge process. The obtained low gravimetric specific capacity is attributed to the large areal mass loading of sulfur. As with previous reports for lithium-ion batteries, thicker electrode cells will be discharged at a higher current density, thus tending to a lower impedance; in addition, a thicker electrode places more strain on the transport of lithium ions in the electrolyte, thus it can possibly decrease the gravimetric specific capacity.[35–40]

Fig. 6b (i) shows that the electrode exhibited well-overlapped and flat plateaus, suggesting good stability and reversibility of the electrode. The initial discharge capacity is relatively low (4.93 mA h cm^{-2} for the electrode and 513 mA h g^{-1} for sulfur) and it can continue to increase until the 11th cycle (6.0 mA h cm^{-2} for the electrode and 625 mA h g^{-1} for sulfur). This behavior can be attributed to the activation step of the S-GS electrode because the surface area of the as-prepared S-GS is low and therefore, it takes a certain amount of time for the electrolyte to flood the internal surfaces of the GO sponges. Only under this condition, the deeply buried sulfur and disulfide bonds can come into contact with the electrolyte and become electrochemically active. Subsequently, the capacities almost stabilized and demonstrated little fading upon extended cycling; as a result, the electrode can exhibit a reversible and

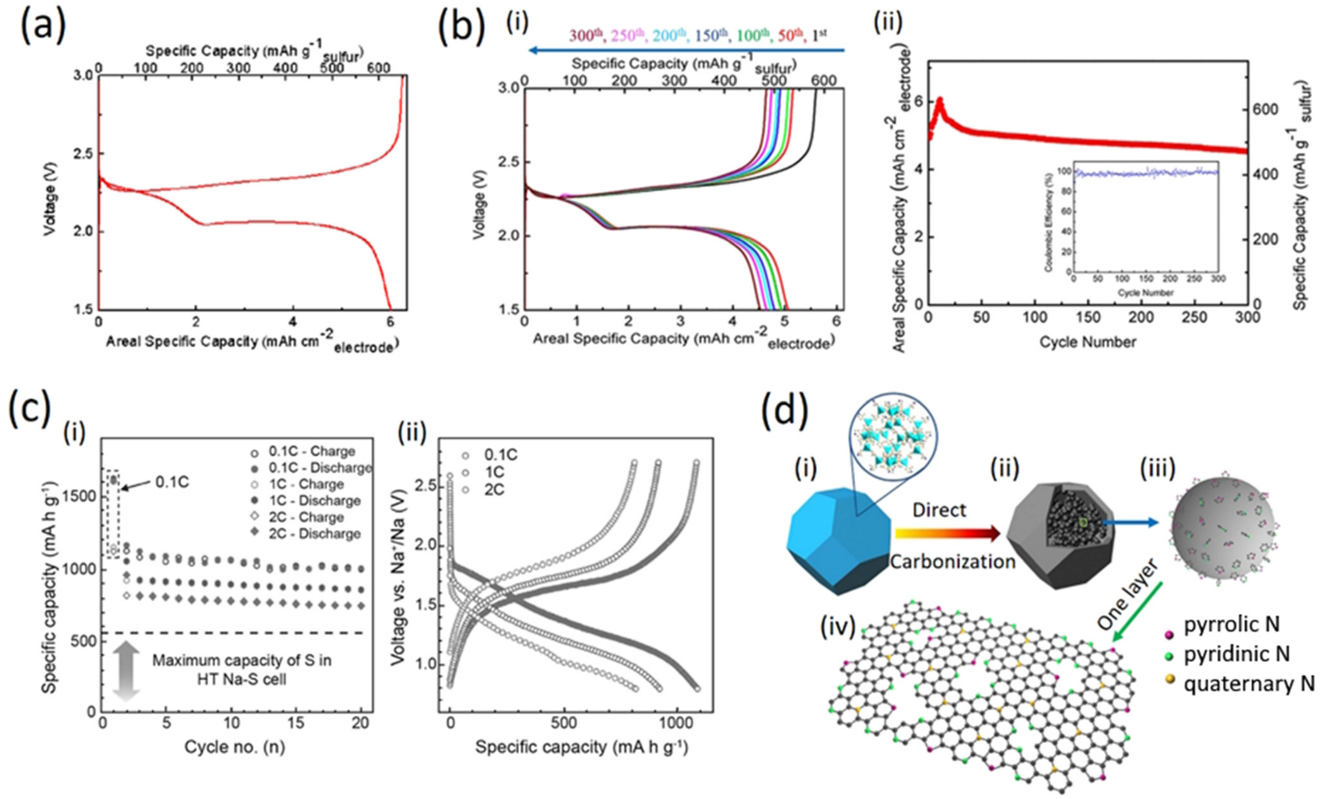

Fig. 6 a) The charge–discharge voltage profiles of the 11th cycle for the S-GS cathode measured during the galvanostatic cycle at 0.1C (with permission from Springer Nature 2014 (ref. 41)); b) i) charge–discharge profiles at different cycle numbers as labelled; (ii) cyclic performance and coulombic efficiency of the S-GS cathode for a Li–S battery at a current density of 0.1C for 300 cycles (with permission from Springer Nature 2014;[41] c) (i) cycling performances and ii) galvanostatic discharge–charge voltage profiles of the S/(CNT@MPC) cathode under different current rates (with permission of Elsevier, 2019);[42] d) schematic illustration of the synthesis procedure of N-doped graphene analogous particles and model of N-doping. (i) ZIF-8. (ii) N-rich carbon polyhedron containing large amounts of graphene analogous particles. (iii) Enlargement of one graphene particle analogue, which contains several graphene layers and can provide abundant active sites at their edges for grafting nitrogen heteroatoms. (iv) The schematic of three types of bonding configurations of N atoms within the hexagonal lattice and edges of a graphene layer (with permission from Springer Nature 2014).[43]

comparable capacity of 4.53 mA h cm^{-2} after 300 cycles; this corresponds to a capacity retention of 75.5% (from its highest capacity of 6.0 mA h cm^{-2}) and the decay rate was as low as 0.08% per cycle for 300 cycles. At the same time, as can be seen from the inserted map in Fig. 6b (ii), the coulombic efficiency remained at around 98%. On the basis of such superior cyclic stability, it is reasonable to conclude that the framework of graphene sponges could effectively improve the cycle stability of the lithium sulfur batteries, likely through absorption and immobilization of the polysulfide intermediate; in fact the framework provides better mechanical support to accommodate the volume changes during charge and discharge.[44–46]

In addition, the sulfur-loaded cathode maintained reversible capacities of ~900 and 800 mA h g^{-1} at distinct rates of 1C and 2C after 20 cycles, respectively. The relation of cycling performance *versus* specific capacity is shown in Fig. 4c (i). The battery exhibited a high reversible capacity after 20 cycles and good rate performance at various current densities of 0.1C, 1C and 2C. The cycling stability and rate capability were improved, but the overall electrochemical performances are not favorable as compared with high temperature solid state NaS batteries mainly due to the solubility of Na_2S_n ($4 \leq n \leq 8$), see Fig. 6c (ii).[41]

2.2 The interactions between nitrogen and graphene

The potential applications of graphene require certain changes in its morphological structure to reach the specifications needed for advanced applications. Among the various strategies proposed to achieve the desired objectives, nitrogen doping, *i.e.*, the incorporation of nitrogen atoms in the carbon lattice, helps to better control the presence of various types of point defects. N-doping can also improve the specific capacitance and cyclability of graphene in supercapacitors as shown in Fig. 6d. Usually, nitrogen doping is preferred in tuning the electronic properties of the C material. Recently, graphene oxide (GO) has been used as a precursor and nine different amino acids are employed as environment-friendly nitrogen sources for the synthesis of nitrogen-doped graphene *via* the hydrothermal method. The product exhibits a polyhedron-like morphology with a diameter of approximately 200 nm (Fig. 6d (i and ii)).

The aggregation of the small graphene analogous particles with the N atoms localized at their edges can generate large amounts of nanopores with their inner surfaces decorated with pyridinic and pyrrolic N, providing more active sites for Li storage and facilitating the transfer of Li ions and electrons in the electrode (Fig. 7a (i and ii)). Thus, the resulting sample shows a higher reversible capacity as an anode material for LIBs than normal N-doped graphene. The divacancy and Stone–Wales defects are inevitably present in the N-doped graphene analogous particles and would be beneficial for the adsorption of Li atoms according to previous reports. However, graphene (capacity of around 568 mA h g^{-1}) and N-doped graphene (900 mA h g^{-1}) both contain divacancy and Stone–Wales defects and exhibited relatively lower capacities for Li storage compared to the different samples (Fig. 7a (iii and iv)), which suggests that the above-mentioned features may contribute to, but not fully cause, any experimentally observed capacity.[47]

Fig. 7b demonstrates that the mesoporous nitrogen-doped carbon-anchored graphene anode derived from melamine as a pore modifier exhibited superior cycle retention and long cycle life for a high power lithium-ion battery. High specific capacities of 775 (after 1100 cycles) and 675 mA h g^{-1} (after 1000 cycles) were obtained at current densities of 1000 and 2000 mA g^{-1} (4C) which are two-fold higher than the initial capacity. The melamine-modified anode exhibited excellent cycle retention of 163% at 1000 mA g^{-1} after 800 cycles, compared to 91% for the unmodified anode, indicating the activation process through the mesoporous channels. The superior and long cycle life was attributed to the melamine-induced features *viz.* mesoporous structure and defective sites formed on carbon/graphene which facilitates efficient electrolyte percolation/ion transport and Li-ion storage, respectively.[40]

In addition, placing a functionalized interlayer between the cathode and the separator helps to reduce the shuttle effects of the soluble Na polysulfide. The Na–S batteries with a Na_2S/activated carbon (AC) nanofiber cathode and carbon-coated pre-sodiated Nafion membrane with high ionic conductivity helped to prevent the migration of the polysulfides to the anode side (Fig. 7c (i)). The respective results show that it took about 8.5 h to accomplish its first

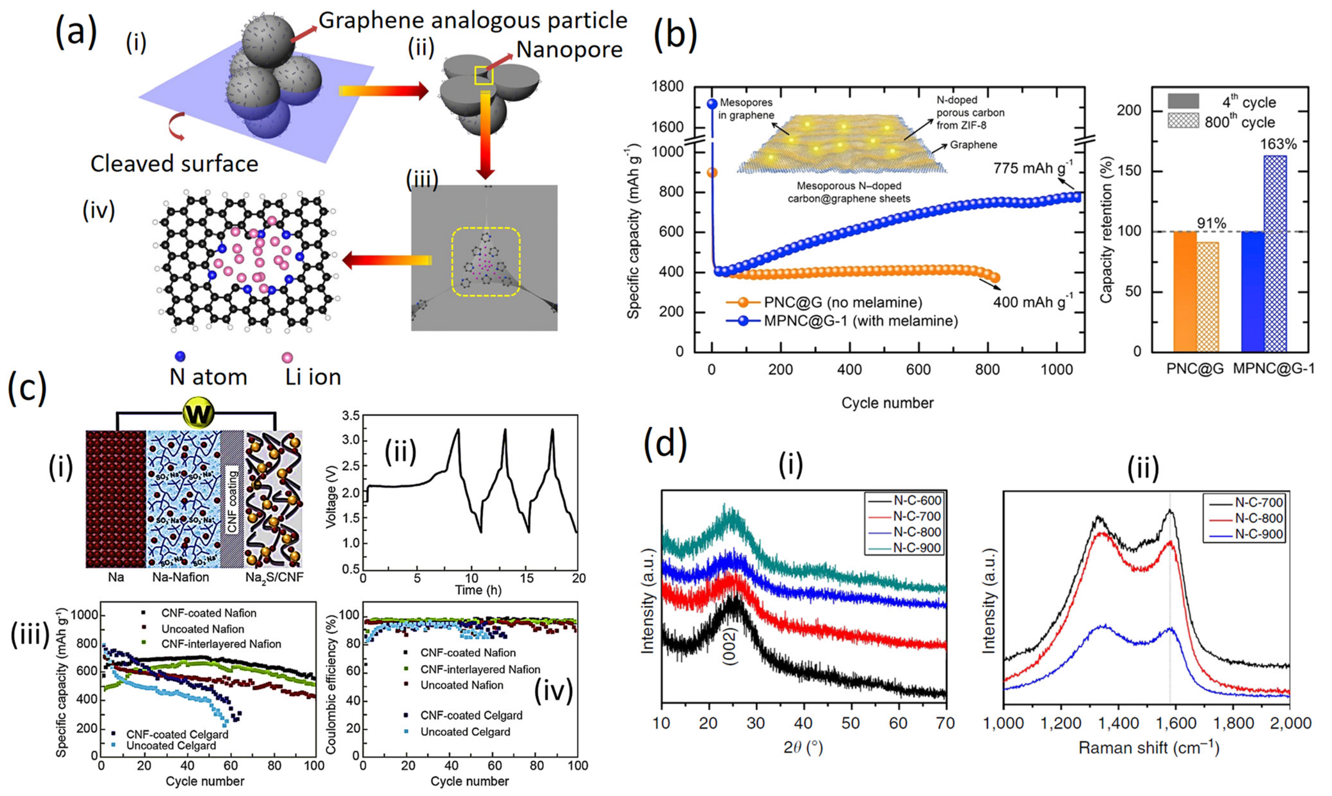

Fig. 7 a) Schematic representation of extra Li storage in N-doped graphene analogous particles. (i) The aggregate of the small graphene analogous particles with N atoms localized at their edges can generate large amounts of nanopores with their inner surface decorated with pyridinic and pyrrolic N, which also provide an extra capacity. (ii) The cleaved surface of the aggregate. (iii) The enlargement of a nanopore between the N-doped graphene analogous particles. (iv) The theoretical calculations model of space for Li storage based on a graphene sheet with a hole containing eight N atoms at the edge (with permission from Springer Nature 2014);[43] b) variation of specific capacity *versus* cycle number with and without a melamine derived nitrogen-doped graphene anode (with permission from Elsevier, 2019);[48] c) i) schematic of a Na-Nafion/AC-CNF coating Na_2S/AC-CNF cell; ii) representative charge/discharge profiles of a NaS battery prepared with a traditional sulfur-carbon cathode; iii) discharge capacities and iv) coulombic efficiencies as a function of cycle number of a Na-Nafion/AC-CNF coating Na_2S/AC-CNF cell (with permission of Elsevier, 2019);[42] d) structural evolution of N-doped graphene analogous particles by XRD and Raman spectroscopy. (i) XRD patterns and (ii) Raman spectra of N-doped graphene-analogous particles obtained at different calcination temperatures (with permission from Springer Nature 2014).[43]

charge process due to the nature of large particle size, high electrical resistivity, and low ion diffusivity of Na_2S. After the Na_2S particles were activated upon a full charge, the subsequent discharge, as well as the following charge–discharge profiles, showed clearly two voltage plateaus, which was similar to the characteristics of the NaS batteries with the conventional elemental sulfur cathodes (Fig. 5c (ii)). The cell displayed a high capacity (over 700 mA h g^{-1}) at C/5 and the cells with the carbon coated Na-Nafion interlayer exhibited a relatively stable coulombic efficiency compared to those of Celgard-cells (Fig. 7c (iii) and (iv)).[49]

The XRD patterns of the N-doped graphene analogous particles (N-C-600, N-C-700, N-C-800 and N-C-900) are shown in Fig. 7d (i). These particles exhibited similar diffraction features with a broad peak at approximately $2\theta = 24°$, corresponding to the carbon (002) peak that is typical of graphitic carbon materials with a low degree of graphitization. No other impurities, such as ZnO or Zn, were observed in the XRD patterns. Fig. 7d (ii) show the Raman spectra for the obtained N-doped graphene analogous particles. The G band is a characteristic feature of graphitic layers, while the D band corresponds to disordered carbon or defective graphitic structures. Raman spectroscopy is sensitive to subtle structural variations in carbon materials. A high I_D/I_G band intensity ratio indicates the generation of large amounts of defects, which suggests that the edge modification of N atoms in graphene-analogous particles occurred in these samples. The I_D/I_G ratio for C-N-800 is greater than that of C-N-700 and C-N-900, demonstrating the presence of more N-doping atoms at the edges of the N-doped graphene-analogous particles. In addition, a broad and weak second-order band was observed at approximately 2700 cm^{-1} for N-C-800 and the shape of the D and 2D bands (more specifically the absence of a typical graphite shoulder) are characteristic features of few-layered graphene.

The CNs structure was characterized by XRD and Raman spectroscopy. All the XRD patterns (Fig. 8a) have two broad diffraction peaks near 25° and 43°, which can be indexed to (002) and (100) planes, respectively. The Raman spectra (Fig. 8b) display two peaks centered at 1353 and 1567 cm^{-1}, corresponding to the disorder-induced D-band and in-plane vibrational G-band, respectively. The intensity ratio of the two peaks, termed as I_G/I_D, can be used to indicate the degree of graphitization.[33] To calculate the I_G/I_D value, it is possible to use the absolute heights of the peaks in the spectra and this value increases at higher temperature, suggesting an elevated graphitization degree; this is in agreement with observations from TEM and XRD. XPS measurements (Fig. 8c and d) indicate that with the increase of temperature, the (002) peak shifts to a higher angle, implying that the graphene interlayer space becomes smaller (Fig. 8e). However, as shown in the relevant sloping discharge profiles (Fig. 8f), the absence of a

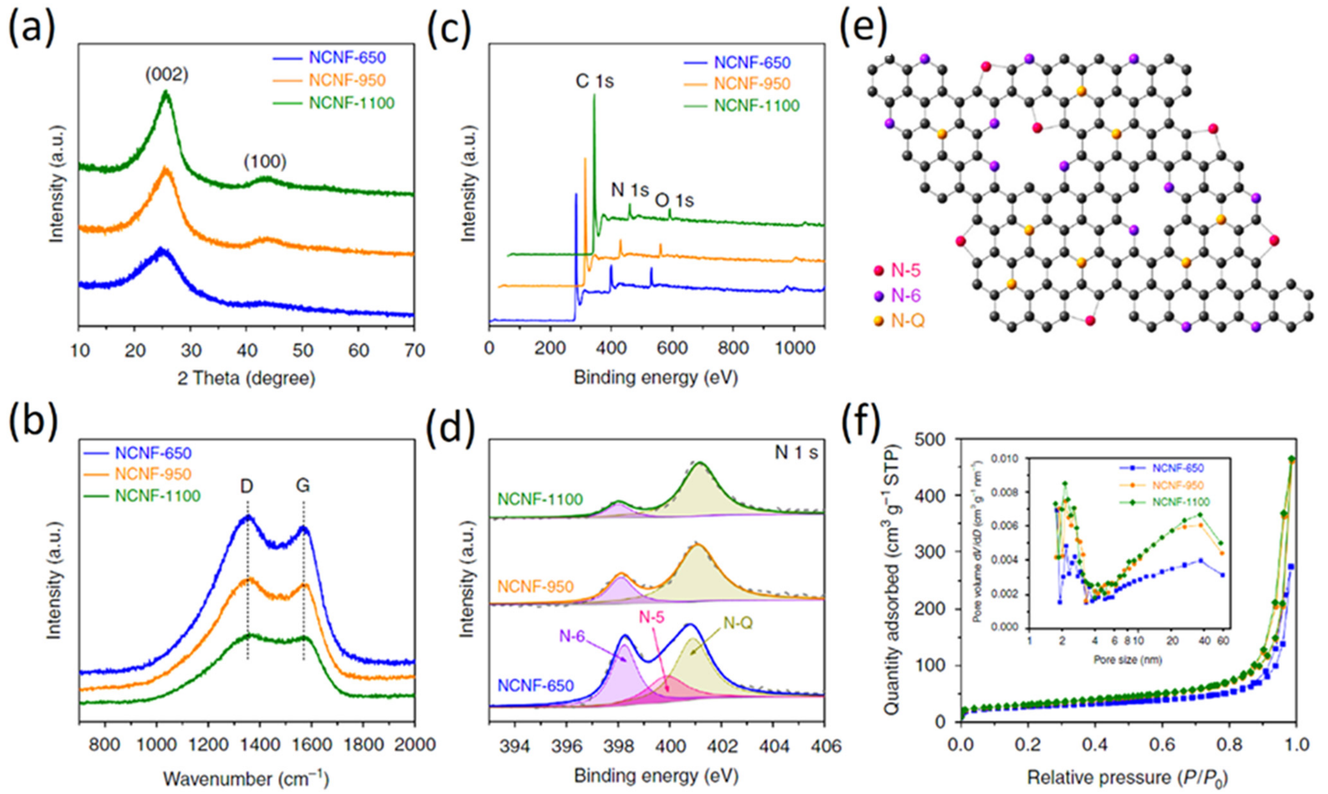

Fig. 8 Structural characterization of NCNFs by different techniques; (a) XRD patterns; (b) Raman spectra; (c) XPS survey spectra; (d) N1s core level XPS high-resolution spectra; (e) scheme illustrating the structure of the N-doping species; (f) nitrogen adsorption–desorption isotherms (inset shows the related pore size distribution) (copyright permission from Springer Nature 2018).[47]

graphite-like low-potential plateau indicates that K-intercalation into graphene layers does not appear to be a major contributor to the overall capacity. A lower *R* value suggests a lower degree of graphitization. The *R* value increases from 2.5 for NCNF-650 to 3.6 and to 4.3 for NCNF-950 and NCNF-1100, respectively, once again confirming the graphitizable nature of the carbons. The overall obtained results show that carbons were prepared by carbonization at different temperatures, showing that the incorporation of nitrogen does not cause any major change in the graphitization.[50–52]

In another report, Esteve-Adell *et al.* added three different graphene nanoplatelet samples into the electrode formulation in a study involving Li-ion batteries. Fig. 9a shows clearly different gas adsorbed quantities for NP1, NP2 and NP3. Micro- and meso-porosity are present in the graphene materials extracted from the isotherm type behaviour and a typical hysteresis cycle can be observed in the desorption process indicating the presence of mesoporous texture in the graphene structure. A BET specific surface area of 296, 470, and 714 $m^2\ g^{-1}$ for NP1, NP2, and NP3, respectively, was calculated. The pore volume shows a small amount of micropores increasing when the specific surface is higher in the following manner: NP3 > NP2 > NP1. A similar pore size distribution is observed for NP1 and NP2; however, substantial differences in pore size distribution are observed for NP3 (Fig. 9a). The GNP with the highest surface area (NP3) has many more mesopores (2–50 nm) and macropores (>50 nm) compared to NP1 and NP2 which leads to a larger average pore diameter of the mesopores in NP3 than in NP1 or NP2. This finding can be attributed to a bigger interlayer space present in NP3.[53]

2.3 Comparison between sulfur- and nitrogen-doped graphene nanoplate electrodes

The excellent electrochemical performance of the A-NSG electrodes is clearly associated with their unique structure. More specifically:

(i) the 3D porous graphene network and graphene layers facilitate electron transfer, and remarkably buffer the volume expansion/contraction of active materials upon cycling. (ii) The inner defects, edges and porous structure not only permit a high sulfur loading in a homogeneously dispersed amorphous state, but they are also beneficial for electrolyte access to the active sulfur component, leading to efficient reactions with Li^+. (iii) Combined physical adsorption of lithium polysulfides onto porous graphene and the chemical binding of polysulfides to N and S sites in the A-NSG promote reversible Li_2S/polysulfide/S conversion, realizing high performance Li–S batteries with long cycle life and high-energy density.

On the other hand, in the high resolution C 1s spectra (Fig. 9b (i–iii)), due to the removal of most oxygen groups as well as the partial reconstruction of the graphitic carbon network, peaks corresponding to C–O (286.2 eV), C═O (288.2 eV) and O–C═O (289.6 eV)[55] decrease considerably for A-NSG, compared with that of GO;[28] two particular new peaks located at 286.1 and 287.2 eV suggest the bond formation of graphene; the sharp peak in the C1s spectrum of A-NSG, still

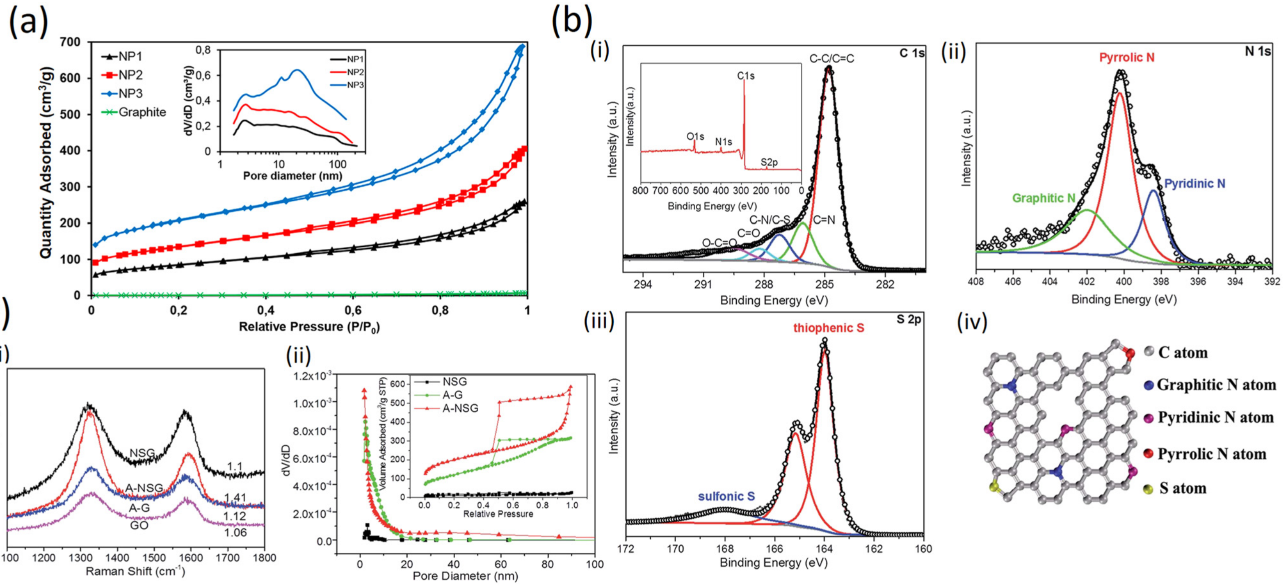

Fig. 9 a) Nitrogen adsorption–desorption isotherms of graphite and three GnPs studied. Inset: Pore size distribution for GnPs (Frontiers publishing 2022, published under open access CC license);[53] b) (i–iii) high-resolution C 1s, N 1s and S 2p XPS spectra of A-NSG and corresponding XPS survey spectra of A-NSG (inset of (i)); (iv) schematic structure of A-NSG with permission from RSC, 2016;[54] c) (i) Raman spectra of GO, NSG, A-G and A-NSG; (ii) pore characterization of the NSG, A-G and A-NSG materials. Inset: adsorbed volume as a function of the relative pressure (with permission from the Royal Society of Chemistry, 2016).[54]

attributed to the sp^2-hybridized graphitic carbon atoms, shifts to higher binding energy and its full width of half-maximum (fwhm) at 284.8 eV increases with the presence of nitrogen content. All these results confirm the formation of C–N bonding configurations in A-NSG. Moreover, in the XPS analysis, the S2p spectrum for the A-NSG nanocomposites in Fig. 9b (iv) has $2p_{3/2}$ and $2p_{1/2}$ spin–orbit levels with an energy separation of 1.27 eV and intensity ratio of 2:1, confirming the effective doping of sulfur atom into the carbon lattice. Two sulfur species are assigned to carbon-bonding: thiophenic S (163.6 eV) and sulfonic S (167.9 eV); the thiophenic S (sulfur atom bonded with carbon directly by a C–S bond) is believed to make the carbon matrix positively charged, thereby increasing its affinity to adsorb polysulfides. At the same time, it is also interesting to find that the C/O ratio of GO is 2.4 and this value increases to 17.52 for A-NSG, indicating that nitrogen-sulfur co-doping increases the reduction efficiency of GO. This seems to be further supported by Raman measurements: in Fig. 9c (i) the Raman spectra for A-NSG exhibit two remarkable peaks at around 1350 and 1580 cm^{-1}. The G band located at 1580 cm^{-1} is related to the E_{2g} vibration mode of sp^2 carbon atoms while the D band at 1350 cm^{-1} is assigned to the defects and disorder hybridized vibrational mode of graphene. Therefore, the higher intensity ratio (I_D/I_G) of A-NSG than GO (1.41 *vs.* 1.06) should be ascribed to the higher amount of defect sites generated by N and S co-doping, resulting in the high disorder of graphene nanosheets as shown in Fig. 9c (ii). More importantly, these defects can provide active sites for lithium polysulfide adsorption.[56]

The structure of the N-CNT and S/N-CNT composites is imaged by TEM as depicted in Fig. 10a (i and ii). One can see from Fig. 10a (i) that N-CNT possesses a typical bamboo-like structure, demonstrating that nitrogen was successfully introduced into the carbon network.[57] During the mixing process of the N-CNT and nano-sulfur aqueous suspension, the surface of N-CNT was mostly occupied by active sulfur for lithium-ion storage. Thus, the diameter of N-CNT increases

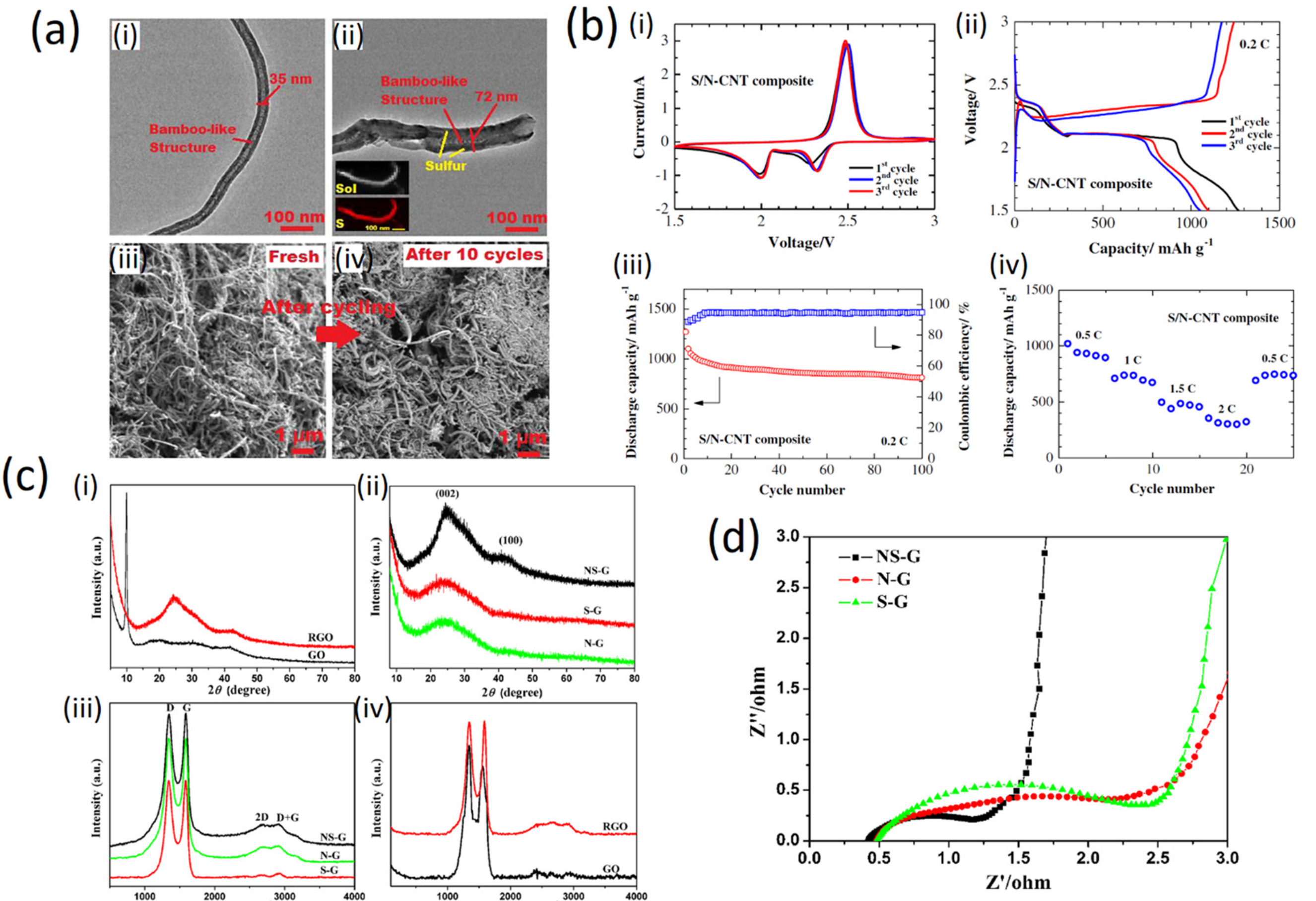

Fig. 10 a) i) and ii) TEM images of N-CNT and S/N-CNT composites. Inset EDS mapping showing the distribution of S in the S/N-CNT composite; iii) and iv) SEM images of the S/N-CNT composite before and after discharge/charge cycles (copyright with permission from Springer, 2015);[49] b) electrochemical performance of (i) a lithium cell with the S/N-CNT composite cathode; i) cyclic voltammograms at 0.1 mV s^{-1} scan rate; ii) discharge/charge profiles at 0.2C; iii) cycling performance of the S/N-CNT composite cathode at 0.2C iv); rate capability of the S/N-CNT composite cathode (with permission of Springer, 2015);[49] c) XRD and Raman characterization patterns of (i) GO and RGO, (ii) NS-G, S-G and N-G respectively. Raman spectra of (iii) NS-G, S-G and N-G, (iv) GO and RGO (with permission from Springer Nature 2015);[24] d) characteristic of real resistance plots of NS-G, N-G and S-G (with permission from Springer Nature 2015).[24]

from 35 to 72 nm. This is in good agreement with the TEM-EDS mapping, which reveals that sulfur coats N-CNT in a uniform manner. Being the core component of the composite, N-CNT can offer a high electronic conductivity and robust framework.[58] Besides, the network-like structure of the S/N-CNT composite favors the penetration of the electrolyte into the cathode.[59] To demonstrate the integrity of the structure of the S/N-CNT composite, comparative SEM imaging of fresh and cycled S/N-CNT composites was conducted. It can be seen from Fig. 10a (iii) and (iv) that the morphology of the S/N-CNT composite does not change remarkably upon cycling and retains its texture. This analysis of micrographs obtained for the fresh and cycled cathodes confirms that the composite was kept rather intact after the cycling, which leads to excellent cyclic stability.

The three initial cyclic voltammetry (CV) curves of a Li/S cell with the S/N-CNT composite cathode are shown in Fig. 10b (i). The CV data evidence two redox processes in the system which agrees well with literature data[60] and could be attributed to the transition of S to polysulfides (Li_2S_8, Li_2S_6, Li_2S_4) and their further transformation to lithium sulfide Li_2S, respectively. In the initial cycles, the activation process associated with the formation of SEI film and the transport of the electrolyte into the porous S/N-CNT composite results in an anodic peak at a slightly lower potential. After this activation, the heights of the main peaks remain at a similar level, indicating good reversibility of the redox processes.

The electrochemical performance of the S/N-CNT composite as a cathode material in Li/S batteries under galvanostatic discharge/charge tests is presented in Fig. 10b (ii). The first plateau at about 2.4 V is related to the formation of higher-order lithium polysulfides (Li_2S_n, $n \geq 4$), which are soluble in the liquid electrolyte. The following electrochemical transition of these polysulfides into lithium sulfide Li_2S is associated to a prolonged plateau around 2.0 V, which well-corresponded with the CV data. Fig. 10b (iii) presents the cycling performance of the S/N-CNT composite at 0.2C. The S/N-CNT composite exhibited a stable cycling behavior with small capacity loss even after 100 cycles. A reversible capacity of 1098 mA h g^{-1} was obtained by the S/N-CNT composite in the second cycle, and the cell retained about 73.5% of its initial reversible discharge capacity after 100 cycles; the coulombic efficiency was maintained above 93%. Based on the above observations, we can conclude that N-CNT could minimize the polysulfide dissolution in a physical and chemical way, thereby stabilizing the capacity significantly. Furthermore, the free-standing S/N-CNT composite film possesses a robust and flexible structure, which could accommodate the solubilization/precipitation of sulfur during the cycles.[37] The rate capability results, as depicted in Fig. 10b (iv), reveal the excellent performance of the S/N-CNT composite at various current densities from 0.5 to 2C. At the initial cycle at 0.5C current, the composite achieves a discharge capacity of 1016 mA h g.[35,36]

The results from XRD measurements are shown in Fig. 10c (i) and (ii). The diffraction peak of GO at $2\theta = 9.9°$ can be assigned to the (002) crystalline plane (Fig. 10c (i)) and the calculated interlayer spacing is about 0.89 nm. This peak entirely disappeared after the hydrothermal reaction. Instead, broad contributions appeared in the freeze-dried RGO (Fig. 10c (i) and doped graphene (Fig. 10c (ii)), indicating the recovery of the π-conjugated system from GO sheets under hydrothermal reaction. As compared to NS-G, the broad and weak contributions of the (002) and (100) in S-G and N-G indicate the poorly ordered graphene sheets along their stacking direction. Using the Bragg equation, the interlayer spacing of NS-G, S-G and N-G was calculated to be 0.36, 0.37 and 0.37 nm, respectively. These values are much lower than that of GO (0.89 nm) but slightly higher than that of graphite (0.335 nm), implying the recovery of a graphitic crystal structure after the hydrothermal reaction.[61,62]

Fig. 10c (iii) and (iv) show the Raman spectra of the prepared samples. All spectra exhibit two main peaks at about 1340 and 1580 cm^{-1} corresponding to the D and G band, respectively. The relative intensities between the D band and G band of NS-G, N-G and S-G seem to be lower than that of GO (Fig. 10c (iii) and (iv)), indicating the recovery of the conjugated network in graphene to a certain extent. Furthermore, the I_D/I_G values of NS-G (0.99), S-G (1.03) and N-G (1.00) are essentially equal, which means that the defect levels of these samples are similar. Electrochemical impedance spectroscopy (EIS) provides information on the internal resistance of the electrode material and the resistance between the electrode and electrolyte. The real part of resistance (Z') measured is the ohmic resistance derived from the electrolyte and the contact between the electrode and the current collector.[34] As shown in Fig. 10d, at very high frequency the internal resistance of the three doped samples is very low (below 0.6 Ω). Hence, the pyrrolic and other nitrogen species in NS-G did not cause a clear increase of resistance, that is different from surface oxygen groups, which often lead to the decrease of conductivity.[63–65]

3. Concluding remarks

Graphene has very strong mechanical properties, but it is also an excellent conductor of heat and electricity and has interesting light absorption abilities. However, synthesis of graphene is required under sulfur-doping conditions to obtain the typical layer-stacked structures with ~100 m^2 g^{-1} SSA as the cathode for NICs. Sulfur-graphene (SG) can deliver almost two times the capacitance of rGO. The electrochemical properties of SG can be ascribed to the layered structures, high carrier mobility and high amount of surface pseudocapacitive functional groups. The beneficial features of SG and NG kinds of doped graphene nanoplatelets render them as particularly promising materials for high-level performance in demanding electrochemical energy storage applications.

Nitrogen-doped graphene exhibits high electrochemical activity towards oxygen reduction in alkali medium providing an affordable industrial alternative for use of metal-based catalysts. The nitrogen and sulfur graphene (NS-G) doped hydrogels and aerogels synthesized through a hydrothermal process using amino acid and graphene oxide as precursors show that the three-dimensional hierarchical structure contains macropores and mesopores with excellent mechanical stability. The simultaneous incorporation of S and N species in the presence of oxygen significantly modified the surface chemistry of carbon leading to considerably higher doping levels, although direct bonding between N and S was not identified. Hence, the synergetic effect between N and S occurred through carbon atoms in neighboring hexagonal rings in a graphene sheet. The enhanced pseudocapacitance in the co-doped samples can be assigned to higher contents of pyrrolic N groups and S species. However, the hybrid GnPs/SWCNTs-S nanocomposite have a high reversible capacity and can be preserved even at a very high current rate, indicating that sulfur in the GnPs/SWCNT-S cathodes helps toward an excellent performance upon use at every current rate. In the future, further fine-tuning of the morphology of graphene nanoplatelets will probably help to decrease the required doping level with S or N, retaining the same or even better performance in the field of energy storage. In this frame, the improvement of the dispersion of N and S in the carbon lattice will also lead to a higher doping efficiency, which will be reflected in the resulting properties and functions of the produced composites.

Conflicts of interest

There are no conflicts to declare.

Acknowledgements

This work was supported by ERC-CZ program (project LL2101) from Ministry of Education Youth and Sports (MEYS) and by project Advanced Functional Nanorobots (reg. No. CZ.02.1.01/0.0/0.0/15_003/0000444 financed by the EFRR).

References

1 S. Liu, V. S. Chevali, Z. Xu, D. Hui and H. Wang, A review of extending performance of epoxy resins using carbon nanomaterials, *Composites, Part B*, 2018, **136**, 197–214.

2 D. Jariwala, V. K. Sangwan, L. J. Lauhon, T. J. Marks and M. C. Hersam, Carbon nanomaterials for electronics, optoelectronics, photovoltaics, and sensing, *Chem. Soc. Rev.*, 2013, **42**, 2824–2860.

3 D. Liu, K. Ni, J. Ye, J. Xie, Y. Zhu and L. Song, Tailoring the Structure of Carbon Nanomaterials toward High-End Energy Applications, *Adv. Mater.*, 2018, **30**, 1802104.

4 J. E. Morris and K. Iniewski, *Graphene, carbon nanotubes, and nanostructures: techniques and applications*, 2013.

5 M. P. Bondarde, R. Jain, J. S. Sohn, K. D. Lokhande, M. A. Bhakare, P. S. Dhumal and S. Some, 23-Carbon-based anode materials for lithium-ion batteries, in *Lithium-Sulfur Batteries*, ed. R. K. Gupta, T. A. Nguyen, H. Song and G. Yasin, Elsevier, 2022, pp. 521–545.

6 H. Zhang, Y. Yang, D. Ren, L. Wang and X. He, Graphite as anode materials: Fundamental mechanism, recent progress and advances, *Energy Storage Mater.*, 2021, **36**, 147–170.

7 D. A. C. Brownson and C. E. Banks, The electrochemistry of CVD graphene: progress and prospects, *Phys. Chem. Chem. Phys.*, 2012, **14**, 8264–8281.

8 L. S. Porto, D. N. Silva, A. E. F. d. Oliveira, A. C. Pereira and K. B. Borges, Carbon nanomaterials: synthesis and applications to development of electrochemical sensors in determination of drugs and compounds of clinical interest, *Rev. Anal. Chem.*, 2019, **38**, 20190017.

9 D. R. Dreyer, R. S. Ruoff and C. W. Bielwaski, From conception to realization: an historial account of graphene and some perspectives for its future, *Angew. Chem., Int. Ed.*, 2010, **49**, 9336–9344.

10 V. Srivastava, Elastic Modulus Micro-Modelling of Graphene Nanoplates (GnPs) Filled Mixture of Epoxy Resin and PVDF Polymer Materials, *Journal of Nanosciences Research & Reports*, 2022, **132**, 2–5, DOI: **10.47363/JNSRR/2022(4)**.

11 O. G. Apul, Q. Wang, Y. Zhou and T. Karanfil, Adsorption of aromatic organic contaminants by graphene nanosheets: Comparison with carbon nanotubes and activated carbon, *Water Res.*, 2013, **47**, 1648–1654.

12 J.-C. Charlier, P. C. Eklund, J. Zhu and A. C. Ferrari, Electron and Phonon Properties of Graphene: Their Relationship with Carbon Nanotubes, in *Carbon Nanotubes: Advanced Topics in the Synthesis, Structure, Properties and Applications*, ed. A. Jorio, G. Dresselhaus and M. S. Dresselhaus, Springer Berlin Heidelberg, Berlin, Heidelberg, 2008, pp. 673–709.

13 Y. Xia, W. Gao and C. Gao, A Review on Graphene-Based Electromagnetic Functional Materials: Electromagnetic Wave Shielding and Absorption, *Adv. Funct. Mater.*, 2022, **32**, 2204591.

14 R. Xu, Z. Wu, S. Zhang, X. Wang, Y. Xia, X. Xia, X. Huang and J. Tu, Construction of All-Solid-State Batteries based on a Sulfur-Graphene Composite and Li9.54Si1.74P1.44S11.7Cl0.3 Solid Electrolyte, *Chem. – Eur. J.*, 2017, **23**, 13950–13956.

15 D. Wei, S. Haque, P. Andrew, J. Kivioja, T. Ryhänen, A. Pesquera, A. Centeno, B. Alonso, A. Chuvilin and A. Zurutuza, Ultrathin rechargeable all-solid-state batteries based on monolayer graphene, *J. Mater. Chem. A*, 2013, **1**, 3177–3181.

16 S. A. Pervez, M. Madinehei and N. Moghimian, Graphene in Solid-State Batteries: An Overview, *Nanomaterials*, 2022, **12**, 2310.

17 H. Kim, K.-Y. Park, J. Hong and K. Kang, All-graphene-battery: bridging the gap between supercapacitors and lithium ion batteries, *Sci. Rep.*, 2014, **4**, 5278.

18 Y. Xiao, Y. Wang, S.-H. Bo, J. C. Kim, L. J. Miara and G. Ceder, Understanding interface stability in solid-state batteries, *Nat. Rev. Mater.*, 2020, **5**, 105–126.

19 R. Kumar, S. Sahoo, E. Joanni, R. K. Singh, K. Maegawa, W. K. Tan, G. Kawamura, K. K. Kar and A. Matsuda, Heteroatom doped graphene engineering for energy storage and conversion, *Mater. Today*, 2020, **39**, 47–65.

20 T. H. Nguyen, D. Yang, B. Zhu, H. Lin, T. Ma and B. Jia, Doping mechanism directed graphene applications for energy conversion and storage, *J. Mater. Chem. A*, 2021, **9**, 7366–7395.

21 H. Wen, B. Guo, W. Kang and C. Zhang, Free-standing nitrogen-doped graphene paper for lithium storage application, *RSC Adv.*, 2018, **8**, 14032–14039.

22 N. Talukder, Y. Wang, B. B. Nunna and E. S. Lee, Nitrogen-doped graphene nanomaterials for electrochemical catalysis/reactions: A review on chemical structures and stability, *Carbon*, 2021, **185**, 198–214.

23 E. Haque, M. M. Islam, E. Pourazadi, M. Hassan, S. N. Faisal, A. K. Roy, K. Konstantinov, A. T. Harris, A. I. Minett and V. G. Gomes, Nitrogen doped graphene via thermal treatment of composite solid precursors as a high performance supercapacitor, *RSC Adv.*, 2015, **5**, 30679–30686.

24 T. Wang, L.-X. Wang, D.-L. Wu, W. Xia and D.-Z. Jia, Interaction between Nitrogen and Sulfur in Co-Doped Graphene and Synergetic Effect in Supercapacitor, *Sci. Rep.*, 2015, **5**, 9591.

25 M.-Q. Zhao, X.-F. Liu, Q. Zhang, G.-L. Tian, J.-Q. Huang, W. Zhu and F. Wei, Graphene/Single-Walled Carbon Nanotube Hybrids: One-Step Catalytic Growth and Applications for High-Rate Li–S Batteries, *ACS Nano*, 2012, **6**, 10759–10769.

26 Z. Xing, B. Wang, J. K. Halsted, R. Subashchandrabose, W. F. Stickle and X. Ji, Direct fabrication of nanoporous graphene from graphene oxide by adding a gasification agent to a magnesiothermic reaction, *Chem. Commun.*, 2015, **51**, 1969–1971.

27 **https://www.graphenea.com/blogs/graphene-news/graphene-role-in-next-generation-lithium-sulfur-batteries**.

28 J. Tian, F. Xing and Q. Gao, Graphene-based nanomaterials as the cathode for lithium-sulfur batteries, *Molecules*, 2021, **26**, 2507.

29 J. Q. Huang, X. F. Liu, Q. Zhang, C. M. Chen, M. Q. Zhao, S. M. Zhang, W. Zhu, W. Z. Qian and F. Wei, Entrapment of Sulfur in Hierarchical Porous Graphene for Lithium-Sulfur Batteries with High Rate Performance from −40 to 60 °C, *Nano Energy*, 2013, **2**, 314–321.

30 S. Yoo, J. Lee, J. M. Kim, K. D. Seong and Y. Piao, Well-dispersed Sulfur Wrapped in Reduced Graphene Oxide Nanoscroll as Cathode Material for Lithium-Sulfur Battery, *J. Electroanal. Chem.*, 2016, **780**, 19–25.

31 T. Lin, Y. Tang, Y. Wang, H. Bi, Z. Liu, F. Huang, X. Xie and M. Jiang, Scotch-Tape-Like Exfoliation of Graphite Assisted with Elemental Sulfur and Graphene-Sulfur Composites for High-Performance Lithium-Sulfur Batteries, *Energy Environ. Sci.*, 2013, **6**, 1283–1290.

32 L. Dai, Functionalization of Graphene for Efficient Energy Conversion and Storage, *Acc. Chem. Res.*, 2013, **46**, 31–42.

33 Y. Feng, H. Zhang, Y. Zhang and X. Qu, C–S Bonds in Sulfur-Embedded Graphene, Carbon Nanotubes, and Flake Graphite Cathodes for Lithium–Sulfur Batteries, *ACS Omega*, 2019, **4**, 16352–16359.

34 X. Wang, X. Li, L. Zhang, Y. Yoon, P. K. Weber, H. Wang, J. Guo and H. Dai, N-doping of graphene through electrothermal reactions with ammonia, *Science*, 2009, **324**, 768–771.

35 Y.-Y. Wang, Z.-W. Zhao, Y. Liu, L.-R. Hou and C.-Z. Yuan, Precipitant-free solvothermal construction of spindle-like CoCO3/reduced graphene oxide hybrid anode toward high-performance lithium-ion batteries, *Rare Met.*, 2020, **39**, 1082–1091.

36 F. Wu, J. Maier and Y. Yu, Guidelines and trends for next-generation rechargeable lithium and lithium-ion batteries, *Chem. Soc. Rev.*, 2020, **49**, 1569–1614.

37 H. F. Xiang, Z. D. Li, K. Xie, J. Z. Jiang, J. J. Chen, P. C. Lian, J. S. Wu, Y. Yu and H. H. Wang, Graphene sheets as anode materials for Li-ion batteries: preparation, structure, electrochemical properties and mechanism for lithium storage, *RSC Adv.*, 2012, **2**, 6792–6799.

38 R. Yang, X.-J. Zhang, T.-F. Fan, D.-P. Jiang and Q. Wang, Improved electrochemical performance of ternary Sn–Sb–Cu nanospheres as anode materials for lithium-ion batteries, *Rare Met.*, 2020, **39**, 1159–1164.

39 B. Zhang, J. Zhou, X. Sun, B. Luo, D. Li, X. Gu and Y. Zhao, Encapsulating Sn(OH)4 Nanoparticles in Micropores of Mesocarbon Microbeads: A New Anode Material for High-Performance Lithium Ion Batteries, *Adv. Mater. Technol.*, 2021, **6**, 2000849.

40 M. D. Stoller, S. Park, Y. Zhu, J. An and R. S. Ruoff, Graphene-Based Ultracapacitors, *Nano Lett.*, 2008, **8**, 3498–3502.

41 S. Lu, Y. Chen, X. Wu, Z. Wang and Y. Li, Three-Dimensional Sulfur/Graphene Multifunctional Hybrid Sponges for Lithium-Sulfur Batteries with Large Areal Mass Loading, *Sci. Rep.*, 2014, **4**, 4629.

42 J. Zhu, J. Zou, H. Cheng, Y. Gu and Z. Lu, High energy batteries based on sulfur cathode, *Green Energy Environ.*, 2019, **4**, 345–359.

43 F. Zheng, Y. Yang and Q. Chen, High lithium anodic performance of highly nitrogen-doped porous carbon prepared from a metal-organic framework, *Nat. Commun.*, 2014, **5**, 5261.

44 J. R. Miller, R. A. Outlaw and B. C. Holloway, Graphene Double-Layer Capacitor with ac Line-Filtering Performance, *Science*, 2010, **329**, 1637–1639.

45 U. N. Maiti, J. Lim, K. E. Lee, W. J. Lee and S. O. Kim, Three-Dimensional Shape Engineered, Interfacial Gelation of Reduced Graphene Oxide for High Rate, Large Capacity Supercapacitors, *Adv. Mater.*, 2014, **26**, 615–619.

46 S. L. Candelaria, Y. Shao, W. Zhou, X. Li, J. Xiao, J.-G. Zhang, Y. Wang, J. Liu, J. Li and G. Cao, Nanostructured carbon for energy storage and conversion, *Nano Energy*, 2012, **1**, 195–220.

47 Y. Xu, C. Zhang, M. Zhou, Q. Fu, C. Zhao, M. Wu and Y. Lei, Highly nitrogen doped carbon nanofibers with superior rate capability and cyclability for potassium ion batteries, *Nat. Commun.*, 2018, **9**, 1720.

48 S. Gayathri, P. Arunkumar, E. J. Kim, S. Kim, I. Kang and J. H. Han, Mesoporous nitrogen-doped carbon@ graphene nanosheets as ultra-stable anode for lithium-ion batteries–Melamine as surface modifier than nitrogen source, *Electrochim. Acta*, 2019, **318**, 290–301.

49 Y. Zhao, F. Yin, Y. Zhang, C. Zhang, A. Mentbayeva, N. Umirov, H. Xie and Z. Bakenov, A Free-Standing Sulfur/Nitrogen-Doped Carbon Nanotube Electrode for High-Performance Lithium/Sulfur Batteries, *Nanoscale Res. Lett.*, 2015, **10**, 450.

50 Á. Caballero and J. Morales, Can the performance of graphene nanosheets for lithium storage in Li-ion batteries be predicted?, *Nanoscale*, 2012, **4**, 2083–2092.

51 J. Wang, J. Liu, D. Chao, J. Yan, J. Lin and Z. X. Shen, Self-Assembly of Honeycomb-like MoS2 Nanoarchitectures Anchored into Graphene Foam for Enhanced Lithium-Ion Storage, *Adv. Mater.*, 2014, **26**, 7162–7169.

52 R. Wang, Y. Hao, Z. Wang, H. Gong and J. T. Thong, Large-diameter graphene nanotubes synthesized using Ni nanowire templates, *Nano Lett.*, 2010, **10**, 4844–4850.

53 I. Esteve-Adell, M. Porcel-Valenzuela, L. Zubizarreta, M. Gil-Agustí, M. García-Pellicer and A. Quijano-Lopez, Influence of the Specific Surface Area of Graphene Nanoplatelets on the Capacity of Lithium-Ion Batteries, *Front. Chem.*, 2022, **10**, 807980.

54 J. Xu, D. Su, W. Zhang, W. Bao and G. Wang, A nitrogen–sulfur co-doped porous graphene matrix as a sulfur immobilizer for high performance lithium–sulfur batteries, *J. Mater. Chem. A*, 2016, **4**, 17381–17393.

55 C. Dai, G. Sun, L. Hu, Y. Xiao, Z. Zhang and L. Qu, Recent progress in graphene-based electrodes for flexible batteries, *InfoMat*, 2020, **2**, 509–526.

56 F. J. Sonia, M. Aslam and A. Mukhopadhyay, Understanding the processing-structure-performance relationship of graphene and its variants as anode material for Li-ion batteries: A critical review, *Carbon*, 2020, **156**, 130–165.

57 F. J. Sonia, M. K. Jangid, B. Ananthoju, M. Aslam, P. Johari and A. Mukhopadhyay, Understanding the Li-storage in few layers graphene with respect to bulk graphite: experimental, analytical and computational study, *J. Mater. Chem. A*, 2017, **5**, 8662–8679.

58 R. Fong, U. Von Sacken and J. R. Dahn, Studies of lithium intercalation into carbons using nonaqueous electrochemical cells, *J. Electrochem. Soc.*, 1990, **137**, 2009.

59 P. Bernardo, J. Dentzer, R. Gadiou, W. Märkle, D. Goers, P. Novák, M. Spahr and C. Vix-Guterl, Influence of graphite surface properties on the first electrochemical lithium intercalation, *Carbon*, 2011, **49**, 4867–4876.

60 K. Ji, J. Han, A. Hirata, T. Fujita, Y. Shen, S. Ning, P. Liu, H. Kashani, Y. Tian, Y. Ito, J.-i. Fujita and Y. Oyama, Lithium intercalation into bilayer graphene, *Nat. Commun.*, 2019, **10**, 275.

61 Z. Niu, J. Chen, H. H. Hng, J. Ma and X. Chen, A leavening strategy to prepare reduced graphene oxide foams, *Adv. Mater.*, 2012, **24**, 4144–4150.

62 F. Liu, S. Song, D. Xue and H. Zhang, Folded structured graphene paper for high performance electrode materials, *Adv. Mater.*, 2012, **24**, 1089–1094.

63 H. Wang, T. Maiyalagan and X. Wang, Review on Recent Progress in Nitrogen-Doped Graphene: Synthesis, Characterization, and Its Potential Applications, *ACS Catal.*, 2012, **2**, 781–794.

64 W. Liu, X. Yan, J. Chen, Y. Feng and Q. Xue, Novel and high-performance asymmetric micro-supercapacitors based on graphene quantum dots and polyaniline nanofibers, *Nanoscale*, 2013, **5**, 6053–6062.

65 S. Guo and S. Dong, Graphene nanosheet: synthesis, molecular engineering, thin film, hybrids, and energy and analytical applications, *Chem. Soc. Rev.*, 2011, **40**, 2644–2672.